Update of a multiphase transport model with modern parton distribution functions and nuclear shadowing

Chao Zhang,[1] Liang Zheng,[2,1] Feng Liu,[1] Shusu Shi,[1,*] and Zi-Wei Lin[1,3,†]

[1]*Key Laboratory of Quark & Lepton Physics (MOE) and Institute of Particle Physics, Central China Normal University, Wuhan 430079, China*
[2]*China University of Geosciences, Wuhan 430074, China*
[3]*Department of Physics, East Carolina University, Greenville, North Carolina 27858, USA*

A multiphase transport (AMPT) model has been successful in explaining a wide range of observables in relativistic heavy ion collisions. In this work, we implement a newer set of free proton parton distribution functions and an impact parameter-dependent nuclear shadowing in the AMPT model. After refitting the parameters of the two-component initial condition model to the experimental data on pp and $p\bar{p}$ total and inelastic cross sections from $\sqrt{s} \sim 4$ GeV to 13 TeV, we study particle productions in pp and AA collisions. We show that the updated AMPT model with string melting can reasonably describe the overall particle yields and transverse momentum spectra for both pp and AA collisions at RHIC and LHC energies after we introduce a nuclear scaling of the minijet transverse momentum cutoff for AA collisions at LHC energies that is motivated by the color glass condensate. Since heavy flavor and high-p_T particles are produced by perturbative-QCD processes and thus directly depend on parton distribution functions of nuclei, the updated AMPT model is expected to provide a more reliable description of these observables.

I. INTRODUCTION

Experimental results from the Relativistic Heavy Ion Collider (RHIC) and the Large Hadron Collider (LHC) [1–3] indicate that a hot and dense medium with partonic degrees of freedom, namely, the quark-gluon plasma (QGP), is created in heavy ion collisions at high energies. To study the properties of QGP, various theoretical methods and models are being developed including a multiphase transport (AMPT) model [4]. The AMPT model aims to describe the whole phase space evolution of heavy-ion collisions as it contains four main components: the fluctuating initial condition, partonic interactions, hadronization, and hadronic interactions. The AMPT model has been widely used to simulate the evolution of the dense matter created in high energy heavy ion collisions. In particular, the string melting version of the AMPT model [4,5], which converts the created matter in the overlap volume into parton degrees of freedom, can well describe the anisotropic flows and particle correlations in collisions of small or large systems at both RHIC and LHC energies [4–8].

However, the current public AMPT model (up to version v1.26/v2.26 [9]) uses the old Duke-Owens parton distribution functions for the free proton and a schematic nuclear shadowing parametrization from the HIJING 1.0 model [10,11]. Therefore, it significantly underestimates the gluon and quark distributions at small x. This would lead to significant uncertainties in its predictions on heavy flavor and/or high-p_T observables, because those particles are initially produced by perturbative-QCD processes and thus directly depend on the parton distribution functions (PDFs) of nuclei. To improve the AMPT model for high energy nuclear collisions, especially on heavy flavor and high-p_T observables, we incorporate in this study a newer set of free proton parton distribution functions (the CTEQ6.1M set [12]) and an impact parameter-dependent EPS09sNLO nuclear shadowing [13] in an updated AMPT model.

The paper is organized as follows. After the introduction, we describe the initial condition of the AMPT model in Sec. II, including the HIJING two-component model, the CTEQ6.1M (NLO) parton distribution functions for the free proton, the impact parameter-dependent EPS09s nuclear shadowing functions, and our determination of the energy dependence of two key parameters (p_0 and σ_{soft}) in the two-component model. We then investigate particle rapidity distributions and transverse momentum spectra from the string melting version of the updated AMPT model in Sec. III, including our results for both pp collisions and AA collisions at RHIC and LHC energies in comparison with the experimental data. More discussions can be found in Sec. IV including the effects of nuclear shadowing and the nuclear scaling of the minijet transverse momentum cutoff p_0 on particle productions in AA collisions. Finally, a summary is given in Sec. V.

II. THE INITIAL CONDITION OF THE AMPT MODEL

The string melting version of a multiphase transport model [4,5] contains four main parts: the fluctuating initial conditions based on the HIJING two-component model [10,11],

---

*shiss@mail.ccnu.edu.cn
†linz@ecu.edu

elastic parton scatterings modeled by the ZPC parton cascade [14], a spatial quark coalescence model to describe the hadronization of the parton matter [5,7], and a hadron cascade based on the ART model [4,15]. When we incorporate new parton distribution functions of nuclei in the AMPT model, two key parameters in the HIJING two-component model, p_0 and σ_{soft}, need to be retuned to describe the cross sections of pp and $p\bar{p}$ collisions.

A. The HIJING two-component model

The HIJING model [10,11], which combines jet production that scales with the number of binary collisions with string fragmentation, provides the initial condition of heavy ion collisions in the AMPT model. In the HIJING model, the primary interactions between the projectile and target are divided into soft and hard components with a transverse momentum scale p_0. An interaction with a momentum transfer larger than p_0 is considered to be a hard process and its production is calculated with perturbative QCD. However, the soft component with a momentum transfer below p_0 is considered to be nonperturbative and characterized by the cross section σ_{soft}.

The inclusive jet differential cross section [16] in HIJING is determined by

$$\frac{d\sigma_{\text{jet}}}{dp_T^2 dy_1 dy_2} = K \sum_{a,b} x_1 f_a(x_1, Q^2) x_2 f_b(x_2, Q^2) \frac{d\sigma^{ab}}{d\hat{t}}, \quad (1)$$

where p_T is the transverse momentum transfer, y_1 and y_2 are, respectively, the rapidity of the two produced partons, x_1 and x_2 are, respectively, the fraction of the momentum carried by the two initial partons, $f_a(x_1, Q^2)$ is the parton distribution function of parton type a at the x value of x_1 and factorization scale Q^2, and σ^{ab} is the cross section between parton types a and b. Note that the K factor in Eq. (1) aims to account for higher-order corrections, since the minijet cross section is calculated at the leading order (even though the PDFs including nPDFs are evaluated at NLO), and the K factor takes the same value (2.5) as in the HIJING1.0 model since version 1.33 and the previous AMPT model for minijet productions. The total inclusive jet cross section (for the production of minijet gluons and $u/d/s$ quarks) is then obtained by integrating the above with a transverse momentum cutoff p_0 [10]:

$$\sigma_{\text{jet}}(s) = \frac{1}{2} \int_{p_0^2}^{s/4} dp_T^2 dy_1 dy_2 \frac{d\sigma_{\text{jet}}}{dp_T^2 dy_1 dy_2}. \quad (2)$$

By introducing a soft interaction cross section σ_{soft}, one can write an eikonal function [17,18] as

$$\chi(b, s) = \tfrac{1}{2} \sigma_{\text{soft}}(s) T_N(b, s) + \tfrac{1}{2} \sigma_{\text{jet}}(s) T_N(b, s), \quad (3)$$

where $T_N(b, s)$ is the partonic overlap function between two nucleons at impact parameter b [10,11]. Then in the eikonal formalism, the total, elastic, and inelastic cross section of the nucleon-nucleon collisions can be written, respectively, as

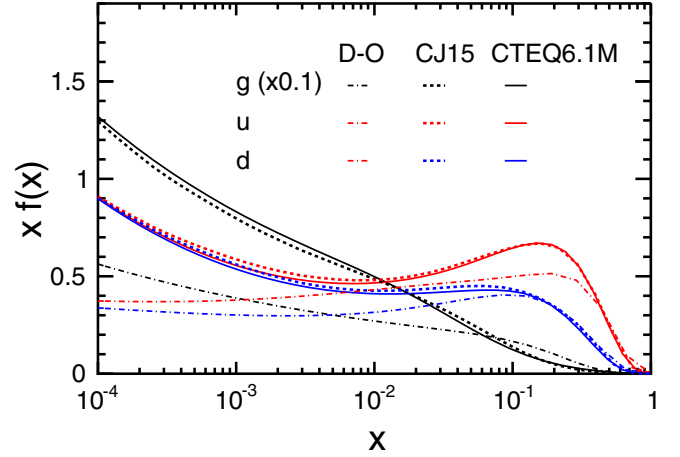$$\sigma_{\text{tot}} = 2\pi \int_0^\infty db^2 [1 - e^{-\chi(b,s)}],$$

FIG. 1. Parton density distributions of the free proton (at $Q^2 = 10$ GeV^2) from the CTEQ6.1M set (solid curves) in comparison with the old Duke-Owens set (dot-dashed) and the more recent CJ15 set (dashed).

$$\sigma_{\text{el}} = \pi \int_0^\infty db^2 [1 - e^{-\chi(b,s)}]^2, \quad (4)$$

$$\sigma_{\text{in}} = \pi \int_0^\infty db^2 [1 - e^{-2\chi(b,s)}],$$

and they depend on both p_0 and σ_{soft}.

B. Parton distribution functions of the free proton

The HIJING 1.0 model in the current AMPT model uses the Duke-Owens parton distribution function set 1 [19] for the free proton. However, it is well known that the Duke-Owens PDFs are outdated, especially when the minijet productions reach the small-x region of the parton distributions at high energies [20]. So in this work we implement the newer CTEQ6.1M set [12] for the parton PDFs of free proton (and free neutron). A similar update of parton PDFs has been done for the HIJING model, where the GRV PDFs [21] were used in the updated HIJING 2.0 model [22] to replace the Duke-Owens PDFs.

Figure 1 compares the parton density distributions (PDFs multiplied by x) from the Duke-Owens, CTEQ6.1M, and CJ15 sets for the gluon, u-quark, and d-quark. Note that the gluon distributions have been scaled down by a factor of ten. We see that all three distributions in the CTEQ6.1M parametrization are quite different from the old Duke-Owens set and are much higher at small x values. In addition, differences between the CTEQ6.1M PDFs and the more recent CJ15 PDFs [23] are quite small.

C. Parton distribution functions in a nucleus

Nuclear shadowing functions describe the modifications of parton distribution functions in a nucleus relative to a simple superposition of parton distribution functions in the nucleon. Since we will be interested in describing nucleus-nucleus collisions at various impact parameters, we implement the impact parameter-dependent EPS09sNLO nuclear
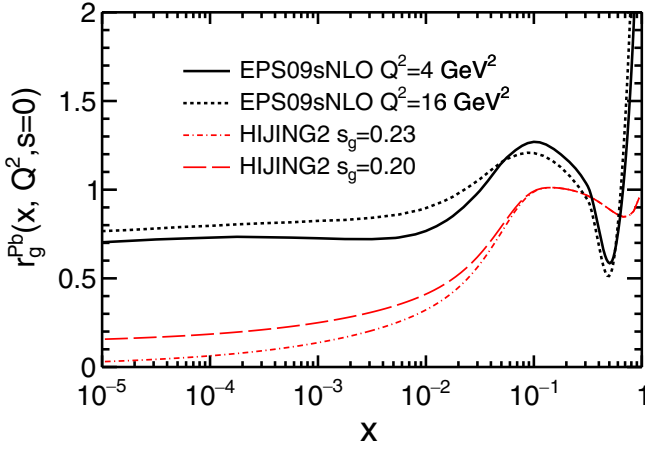
FIG. 2. Comparison of the nuclear shadowing functions of gluons at the center of a lead nucleus from the EPS09s NLO set at two different Q^2 values and from the HIJING 2 parametrization with two different values for the s_g parameter.

shadowing functions [13] instead of the spatially independent (averaged) EPS09 nuclear shadowing [24]. They describe the spatial dependence of nuclear PDFs (nPDFs) and are based on data from deep inelastic lepton-nucleus scatterings, Drell-Yan dilepton productions, and specifically pion productions measured at RHIC [25] which improve the determination of the gluon densities. Note that the EPS09sNLO set was calculated with the CTEQ6M set as the free proton PDFs, which is almost equivalent in every respect to the CTEQ6.1M set [26].

For an average bound proton in a nucleus, the distribution function of parton flavor i can be written as

$$f_i^{p/A}(x, Q^2) \equiv R_i^A(x, Q^2) f_i^p(x, Q^2), \qquad (5)$$

where $f_i^p(x, Q^2)$ is the corresponding PDF in the free proton. Here $R_i^A(x, Q^2)$ represents the spatially-averaged nuclear modification or shadowing function, which mainly contains three effects depending on the x range: the shadowing effect, anti-shadowing effect, and the EMC effect. It is an integral of the spatially dependent nuclear shadowing function as given by

$$R_i^A(x, Q^2) \equiv \frac{1}{A} \int d^2\mathbf{s}\, T_A(\mathbf{s})\, r_i^A(x, Q^2, \mathbf{s}). \qquad (6)$$

In the above, $T_A(\mathbf{s})$ is the nuclear thickness function at transverse position $\mathbf{s}$, and $r_i^A(x, Q^2, \mathbf{s})$ is the spatially dependent nuclear shadowing.

Figure 2 shows the gluon shadowing functions at the center of a lead nucleus from the EPS09s NLO set at two different Q^2 values and from the HIJING 2.0 model at two different s_g values suggested for LHC energies [22]. We see that the EPS09sNLO gluon shadowing at small x is much weaker than the HIJING shadowing. Note that the current AMPT model uses the HIJING 1.0 nuclear shadowing parametrization, which is spatially dependent but independent of Q^2 or the parton flavor [4,10] and similar to the HIJING 2.0 nuclear shadowing.
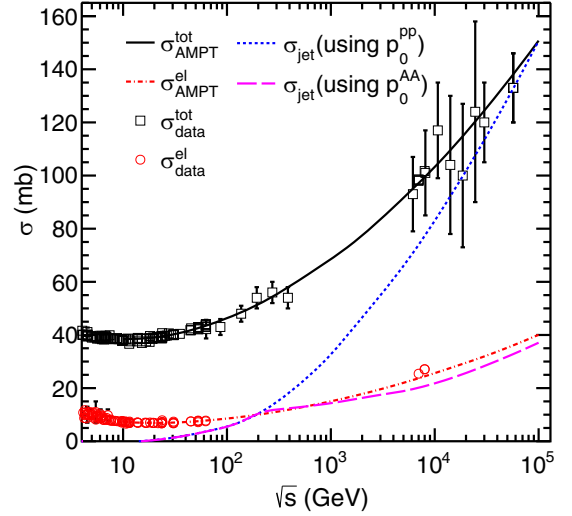

FIG. 3. Total and elastic cross sections versus the colliding energy of pp collisions from the experimental data (symbols) in comparison with the AMPT results (solid and dot-dashed curves); jet cross section per pp collision, $\sigma_{\rm jet}$, is also shown for pp (dotted) and AA (dashed) collisions.

D. Fitting the two-component model to pp and $p\bar{p}$ cross section data

The two parameters, p_0 and $\sigma_{\rm soft}$, in the HIJING 1.0 model directly affect the total and inelastic cross sections of pp and $p\bar{p}$ collisions, as shown in Sec. II A. In the current AMPT model that uses the Duke-Owens PDFs, constant values of $p_0 = 2.0$ GeV/c and $\sigma_{\rm soft} = 57$ mb (at high energies [27]) are found to be able to describe the experimental cross sections of pp and $p\bar{p}$ collisions [10,11]. This is no longer the case after we use the CTEQ PDFs here, or when the GRV PDFs were used for the HIJING 2.0 model [22]. Instead, energy-dependent $p_0(s)$ and $\sigma_{\rm soft}(s)$ values are needed.

Again we use the experimental total and inelastic cross sections of pp and $p\bar{p}$ collisions within the energy range $4 < \sqrt{s} < 10^5$ GeV, as shown in Fig. 3, to determine these two parameters at a given energy. To fit the experimental cross sections, we minimize the sum of squared relative difference between the model results and the cross section data points. We then determine the following fit functions of $p_0(s)$ and $\sigma_{\rm soft}(s)$:

$$p_0^{pp}(s) = -1.71 + 1.63 \ln(\sqrt{s}) - 0.256 \ln^2(\sqrt{s})$$
$$+ 0.0167 \ln^3(\sqrt{s}), \qquad (7)$$

$$\sigma_{\rm soft}(s) = 45.1 + 0.718 \ln(\sqrt{s}) + 0.144 \ln^2(\sqrt{s})$$
$$+ 0.0185 \ln^3(\sqrt{s}). \qquad (8)$$

In the above, p_0^{pp} and $\sigma_{\rm soft}$ are in the unit of GeV/c and mb, respectively; while the center-of-mass colliding energy $\sqrt{s}$ is in the unit of GeV. Note that we have denoted the above minijet transverse momentum cutoff as p_0^{pp} because it represents the p_0 fit function for pp collisions, while we shall see in Sec. III B that p_0 needs to be A-dependent to reproduce the particle yields in AA collisions at very high energies such as LHC energies. Also, p_0 values are only relevant when the
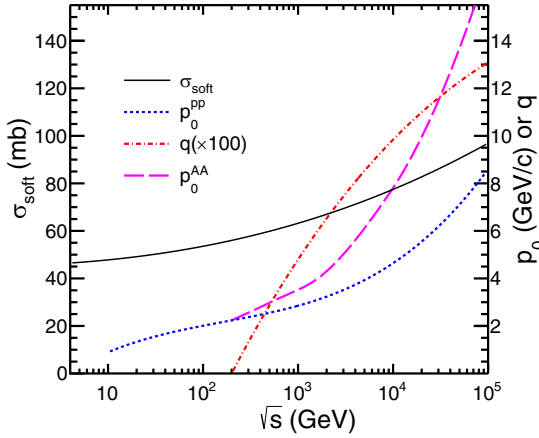
FIG. 4. Fitted σ_{soft} function (solid curve), p_0^{pp} function for pp collisions (dotted), and the q function (dot-dashed, scaled up by a factor of 100) versus the colliding energy. Dashed curve represents the p_0^{AA} function for central AA collisions after the nuclear scaling of p_0 of Eq. (10). Note that p_0 is only relevant at $\sqrt{s_{NN}} > 10$ GeV.
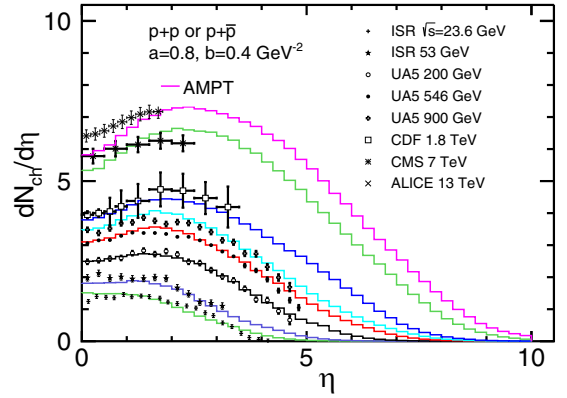

FIG. 5. Pseudorapidity distributions of charged particles in NSD pp collisions at $\sqrt{s} = 7$ TeV [29], NSD $p\bar{p}$ collisions at 200, 546, 900 [30], and 1800 GeV [31], and inelastic pp collisions at 23.6 GeV, 53 GeV [32], and 13 TeV [33] from AMPT (curves) in comparison with the experimental data.

center-of-mass energy per nucleon-pair is higher than 10 GeV, because the jet production in the HIJING model is switched off at $\sqrt{s} < 10$ GeV.

Figure 4 shows these two fit functions versus the colliding energy. We see that both show a strong energy dependence, especially the minijet cutoff scale p_0. Because the CTEQ parametrization has much higher gluon densities at small x than the Duke-Owens PDFs, it has a larger jet cross section at high colliding energies, therefore a higher p_0 value than the previous value of 2 GeV/c is needed to reproduce the total and elastic cross section data at high energies. As shown in Fig. 3, the above fit functions of $p_0(s)$ and $\sigma_{\text{soft}}(s)$ allow the updated AMPT model to describe the experimental data on the total and elastic cross sections of pp collisions within a wide energy range $4 < \sqrt{s} < 10^5$ GeV.

III. RESULTS ON PARTICLE PRODUCTIONS

We now study particle productions in pp and AA collisions with the string melting version of the updated AMPT model and compare with the experimental data. In the string melting AMPT model [4,5], the initial partons are produced through the intermediate step of Lund string fragmentation, where hadrons and resonances from the fragmentation process are decomposed into (anti)quarks according to the quark model. Therefore, the initial phase-space distribution of the produced partons depends on the string fragmentation parameters, particularly the a and b parameters in the Lund symmetric fragmentation function:

$$f(z) \propto z^{-1}(1-z)^a \exp(-bm_T^2/z). \quad (9)$$

In the above, z is the light-cone momentum fraction of the produced hadron with respect to the fragmenting string, and m_T is the hadron transverse mass. As a result, the final spectrum of produced particles in the AMPT model depends on the Lund a and b parameters [4,28]. In particular, a smaller Lund b value leads to a harder p_T spectrum [28]. Note that

the updated AMPT model used for this study also includes the new quark coalescence [7], which respects the net-baryon conservation in each event but does not force the numbers of mesons, baryons, and antibaryons in an event to be separately conserved through the quark coalescence process. In this study, the r_{BM} parameter in the new coalescence, which controls the relative probability of a quark forming a baryon instead of forming a meson, is set to 0.53 for $u/d/s$ quarks. In addition, the parton cross section in ZPC is set to 3 mb.

In this section, we first investigate particle productions in pp collisions at RHIC and LHC energies to determine the values of the Lund a and b parameters. We then apply the same Lund a and b values as well as the same minijet cutoff value p_0 to AA collisions, and we shall see that they fail to describe the experimental data of central AA collisions. We then keep the same Lund a value but determine the Lund b value and the A-scaled p_0 value that are needed for the string melting AMPT model to reproduce the overall particle productions in central AA collisions at RHIC and LHC energies.

A. Particle productions in pp collisions

With the $p_0^{pp}(s)$ minijet cutoff function, using constant Lund fragmentation parameters of $a = 0.8$ and $b = 0.4$ GeV^{-2} allows the string melting AMPT model to reasonably describe the pp and $p\bar{p}$ data in both the $dN_{ch}/d\eta$ distributions and the p_T spectra. Figure 5 shows charged particle pseudo-rapidity distributions from the updated AMPT model in comparison with the experimental data of pp and $p\bar{p}$ collisions from $\sim$20 GeV to 13 TeV. Note that we use the same procedure to select events for the AMPT analysis as that used for the experimental data. For example, NSD events in the UA5 data refer to events that contains at least one hit simultaneously on both sides of the chambers covering $2 < |\eta| < 5.6$, while for the CDF and CMS data they refer to the ranges of $3.2 < |\eta| < 5.9$ and $2.9 < |\eta| < 5.2$, respectively.

Figure 6 shows the transverse momentum spectra of charged particles in pp and $p\bar{p}$ collisions from the string melting AMPT model at different colliding energies in
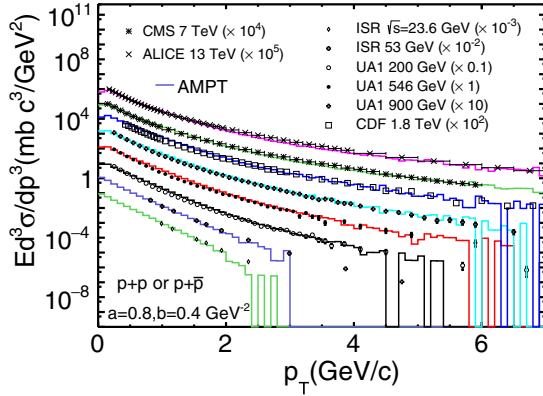
FIG. 6. Invariant cross sections of charged particles versus p_T in pp collisions at $\sqrt{s} = 23.6$ and 53 GeV [32], $p\bar{p}$ collisions at 200, 546, 900 [34], and 1800 GeV [35], and pp collisions at 7 [36] and 13 TeV [37] from the AMPT model in comparison with the experimental data.

comparison with data. Note that for $\sqrt{s} = 7$ and 13 TeV, we have converted the data on Ed^3N/dp^3 to $Ed^3\sigma/dp^3$. We have used the same η range in calculating the AMPT results as that in the experimental data: $|\eta| < 0.35$ for $\sqrt{s} = 23.6$ and 53 GeV, $|\eta| < 2.5$ for 200, 546, and 900 GeV, $|\eta| < 1$ for 1.8 TeV, $|\eta| < 0.8$ for 7 TeV, and $|\eta| < 2.4$ for 13 TeV.

For identified particles, we compare in the upper panel of Fig. 7 the string melting AMPT results on dN/dy at midrapidity for pions, kaons, protons, and antiprotons in pp collisions as functions of the colliding energy from 6 GeV to 13 TeV. The experimental data are shown by symbols for comparison. We see that the string melting AMPT model can reasonably describe the energy dependence of most of these hadrons, including the fast increase of the antiproton yields with the colliding energy and the nonmonotonous energy dependence of the proton dN/dy.
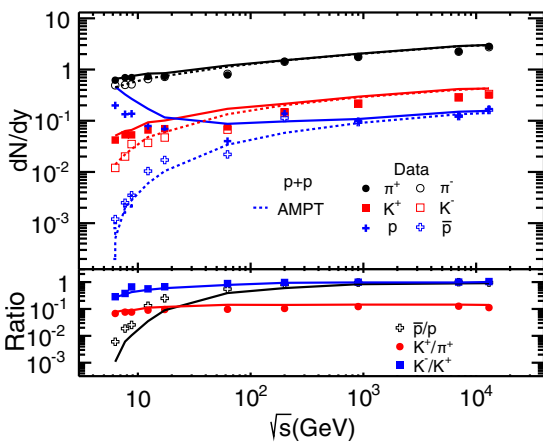

FIG. 7. Identified particle dN/dy and particle ratios at midrapidity in pp collisions versus the colliding energy; curves represent the AMPT results with $a = 0.8$ and $b = 0.4$ GeV^{-2}, while symbols represent the experimental data from NA61SHINE [38], PHENIX [39], STAR [40], and ALICE [41–43].

We also see from Fig. 7 that charged pion and kaon productions from the AMPT model show good consistency with the pp experimental data at different colliding energies, including the K^+/π^+ and K^-/K^+ ratios as functions of the colliding energy as shown in the lower panel of Fig. 7. However, the AMPT model here underestimates the antiproton yield and overestimates the proton yield at lower colliding energies. As a result, the $\bar{p}/p$ ratios from the AMPT model are lower than the data at the lower RHIC energies. Note that in Fig. 7 the PHENIX proton and antiproton data [39] shown at 62.4 GeV are corrected for feed-down effects, but the STAR proton and antiproton data [40] shown at 200 GeV are not.

B. Particle productions in AA collisions

Now we investigate results from the updated AMPT model on particles productions in nucleus-nucleus collisions. First we take the same parameters as for pp collisions, i.e., Lund fragmentation parameters $a = 0.8$, $b = 0.4$ GeV^{-2}, and the $p_0^{pp}(s)$ minijet cutoff function. Figure 8 shows the dN/dy (left panels) and p_T spectra (right panels) of π^+, K^+, p, and $\bar{p}$ for 0–5% central Au + Au collisions at $\sqrt{s_{NN}} = 200$ GeV and 0–5% central Pb + Pb collisions at 2.76 TeV, where results from the updated AMPT model are being compared to the experimental data [44–46]. Note that we show the PHENIX proton and antiproton data because they have been corrected for feed-down effects. Also, the kaon and (anti)proton dN/dy values from both the model and the experimental data have been multiplied by a constant factor for easier identification.

We see from Fig. 8 that the updated AMPT model with $a = 0.8$, $b = 0.4$ GeV^{-2}, and the $p_0^{pp}(s)$ minijet cutoff significantly overestimates the yields of most of these particles for central heavy ion collisions at both RHIC and LHC energies. Also, the p_T spectra of these particles from the AMPT model are mostly softer than the data for both collision systems. Moreover, with the p_0^{pp} minijet cutoff and EPS09sNLO nuclear shadowing, we find it impossible to reproduce the overall particle yields of Pb + Pb collisions at LHC energies regardless of the Lund a and b values.

We thus introduce the following A-scaling of p_0, which increases the minijet cutoff p_0 for central AA collisions at high energies such as the LHC:

$$p_0^{AA} = p_0^{pp} A^{q(s)}, \tag{10}$$

$$q(s) = 0.0334 \ln\left(\frac{\sqrt{s}}{200}\right) - 0.00232 \ln^2\left(\frac{\sqrt{s}}{200}\right)$$

$$+ 0.0000541 \ln^3\left(\frac{\sqrt{s}}{200}\right), \quad \text{for } \sqrt{s} \geqslant 200 \text{ GeV}. \tag{11}$$

In the above, $\sqrt{s}$ refers to $\sqrt{s_{NN}}$ in AA collisions and is in the unit of GeV. This $q(s)$ fit function is shown in Fig. 4, where it is zero at $\sqrt{s_{NN}} \leqslant 200$ GeV, reaches a value of 0.13 at $\sqrt{s_{NN}} = 10^5$ GeV, and approaches 0.16 at $\sqrt{s_{NN}} \sim 10^7$ GeV. The nuclear-scaled p_0 function, p_0^{AA}, is also shown in Fig. 4, where we can see the significant increase of the cutoff scale p_0 in central AA collisions at LHC energies and beyond. The above nuclear scaling of the minijet momentum cutoff scale p_0 is motivated by the physics of color glass condensate [47],
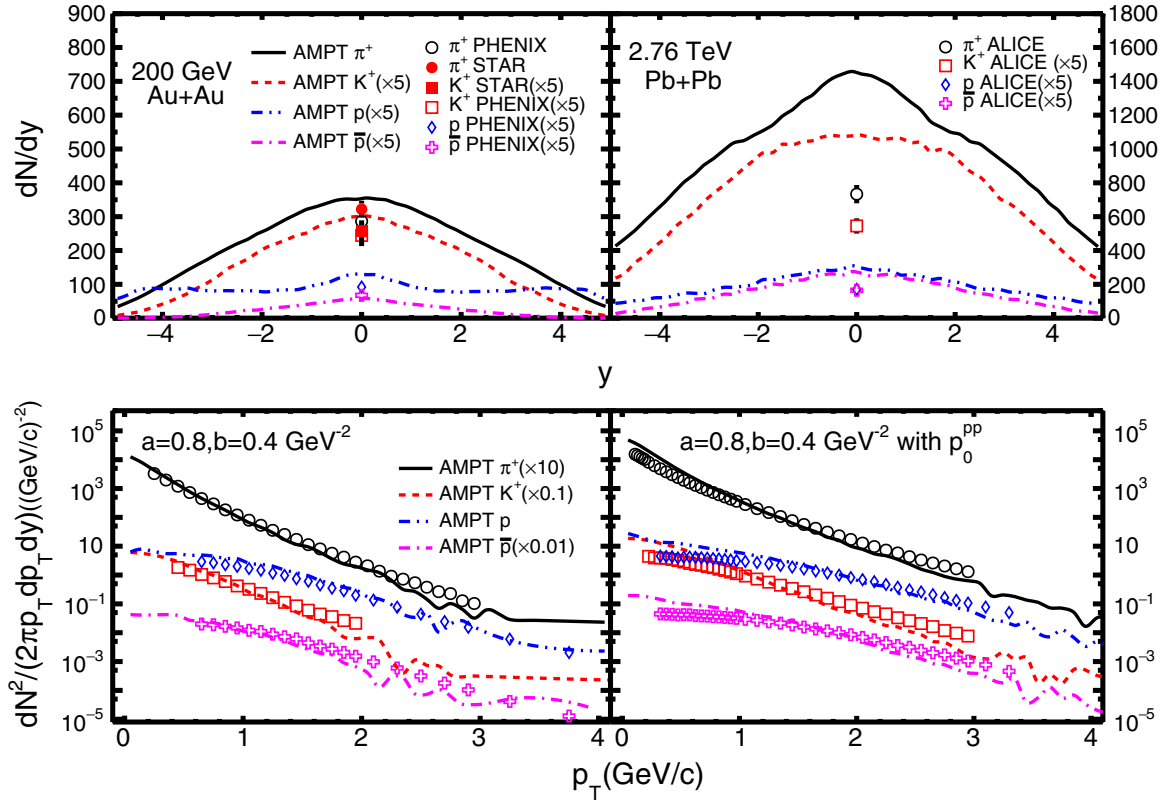
FIG. 8. Identified particle dN/dy distributions (upper panels) and p_T spectra (lower panels) for 0–5% central Au + Au collisions at 200 GeV (left panels) and 0–5% central Pb + Pb collisions at 2.76 TeV (right panels). Curves represent the AMPT results using the same Lund fragmentation parameters and p_0 as for pp collisions, while symbols represent experimental data [44,46].

where the saturation momentum scale Q_s depends on the nuclear size as $Q_s \propto A^{1/6}$ in the saturation regime for small-x gluons in AA collisions at high-enough energies.

To obtain the above $q(s)$ fit function, first we decide to keep using the EPS09s nuclear shadowing, although it has significant uncertainties on its gluon shadowing function at small x [13]. We also use the same Lund a value of 0.8 for AA collisions as for pp collisions, unlike in studies with the previous AMPT model [4,7]. In addition, we find that a significantly smaller value for the Lund b parameter, $b = 0.15$ GeV^{-2}, is needed to describe particle productions in AA collisions. This was also the case for the previous string melting version of the AMPT model [6,28]. Note that throughout this study we use the default PYTHIA value of 0.30 for the relative production of strange to nonstrange quarks, instead of imposing an upper limit of 0.40 as done for the string melting version of the previous AMPT model [28]. We then use the overall particle yields of central Au + Au collisions at the higher RHIC energies and central Pb + Pb collisions at LHC energies to determine the corresponding q value at each energy, and finally a fit of the obtained q values is done to arrive at the above $q(s)$ fit function.

Figure 9 shows the dN/dy distributions (left panels) and p_T spectra (right panels) from the AMPT model using the new Lund b parameter and $p_0^{AA}(s)$ cutoff in comparison with the experimental data. We see that most of the dN/dy data

of π^+, K^+, p, and $\bar{p}$ in these central heavy ion collisions can now be reasonably reproduced. The p_T spectra are also much harder than those in Fig. 8 and mostly consistent with the corresponding heavy ion data, due to the smaller value of the Lund b parameter [28].

In Fig. 10, the energy dependencies of identified particle yields at midrapidity are shown in the upper panel for 0–5% central Au + Au collisions at RHIC energies and 0–5% central Pb + Pb collisions at LHC energies. The corresponding particle ratios are shown in the lower panel. Note that the rapidity range at 2.76 TeV is $|y| < 0.5$ while at other energies is $|y| < 0.1$, and that the PHENIX (anti)protons data at 62.4 and 130 GeV are not corrected for feed-down from weak decays. We see from Fig. 10 that the yields of charged pions and kaons as well as their ratios are well reproduced by the updated AMPT model. However, similar to the trend in pp collisions, at lower energies the string melting AMPT model underestimates the antiproton yield but tends to overestimates the proton yield at midrapidity. As a result, the midrapidity $\bar{p}/p$ ratios from the string melting AMPT model at the lower RHIC energies are significantly smaller than the experimental data. However, the AMPT model can reasonably reproduce the (anti)proton data for central Pb + Pb collisions at the LHC energy of 2.76 TeV. These features are similar to those in the earlier study that used the previous string melting AMPT model with the new quark coalescence [7].
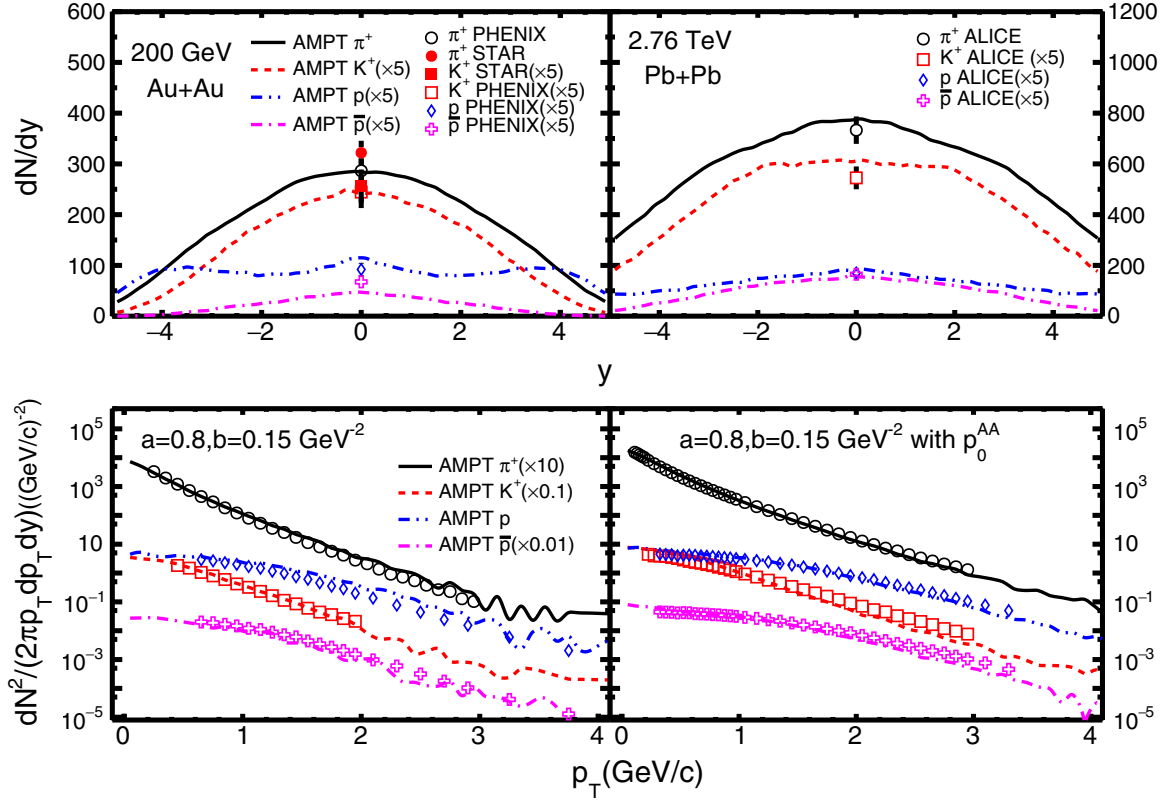
FIG. 9. Same as Fig. 8 but using Lund $b = 0.15$ GeV^{-2} and A-scaled minijet cutoff $p_0^{AA}(s)$ for central AA collisions; note that $p_0^{AA} = p_0^{pp}$ at $\sqrt{s_{NN}} = 200$ GeV.

IV. DISCUSSIONS

Since the EPS09s nuclear shadowing is impact parameter-dependent and diminishes for nucleons near the edge of the nucleus, we expect the effect of nuclear shadowing to depend on centrality and vanish for very peripheral AA collisions. This is shown in Fig. 11 by the centrality dependence of charged particle $dN/d\eta$ within $|\eta| < 0.5$ divided by $N_{\rm part}/2$ for Au + Au collisions at 200 GeV (thin curves, data from Ref. [49]) and Pb + Pb collisions at 2.76 TeV and 5.02 TeV (medium and thick curves, respectively, data from Ref. [50]
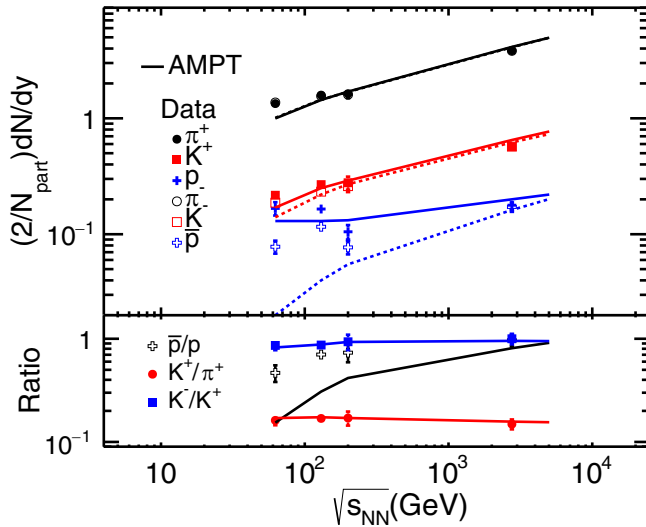

FIG. 10. Identified particle dN/dy and particle ratios at midrapidity in 0–5% central Au + Au or Pb + Pb collisions versus the colliding energy; curves represent AMPT results, while symbols represent experimental data at 62.4 GeV [45], 130 GeV [48], 200 GeV [44], and 2.76 TeV [46].
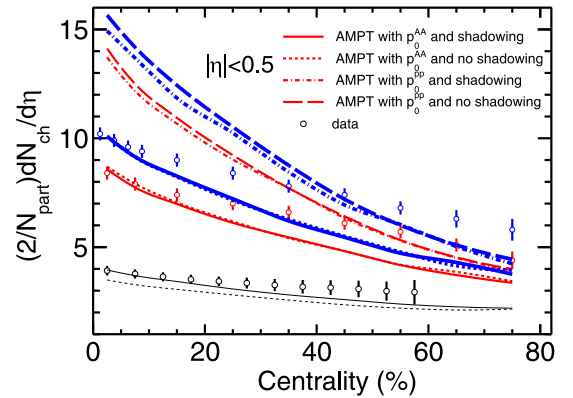

FIG. 11. Centrality dependence of midrapidity $dN_{ch}/d\eta$ divided by $N_{\rm part}/2$ from the AMPT model for Au + Au collisions at 200 GeV and Pb + Pb collisions at 2.76 TeV and 5.02 TeV with (solid) and without (dotted) nuclear shadowing in comparison with data [49–51]. Also shown are AMPT results at LHC energies without using the A-scaling of p_0 for central AA collisions with (dot-dashed) or without (dashed) nuclear shadowing, which are applicable to very peripheral AA collisions.

and Ref. [51], respectively). Note that centrality is determined according to the number of charged particles detected by the beam-beam counters that cover $3.0 < |\eta| < 3.9$ at 200 GeV or by the V0 detectors that cover $2.8 < \eta < 5.1$ and $-3.7 < \eta < 1.7$ at 2.76 TeV or 5.02 TeV. The same centrality criterion is used in the analysis of our model results, and we take N_{part} as the total number of nucleon participants from both the projectile and target nuclei due to inelastic collisions in the AMPT calculations.

As expected, we see in Fig. 11 that the shadowing effect is very small for peripheral collisions. Actually, the figure shows that nuclear shadowing has a small effect on charged particle yields at all centralities for AA collisions from the top RHIC energy to LHC energies. This is because of the large p_0 values at high energies as shown in Fig. 4 as well as the relatively weak EPS09sNLO nuclear shadowing at large Q^2 values as shown in Fig. 2. A large p_0 value suppresses the minijet component's contribution, which is sensitive to the nuclear shadowing, to the particle yields relative to the soft component's contribution. If the nuclear scaling of p_0 is not applied, we can see in Fig. 11 that nuclear shadowing would reduce the overall particle yields by a finite (but still small) amount for central Pb + Pb collisions at LHC energies, because p_0^{pp} is significantly lower than p_0^{AA} there.

However, Fig. 11 shows that the A-scaling of p_0 has a large effect on charged particle yields in AA collisions at LHC energies, especially for more central collisions. As mentioned earlier, the string melting AMPT model significantly overestimates the charged particle yields in central Pb + Pb collisions at LHC when it uses p_0^{pp}, the same minijet cutoff scale as for pp collisions. After the A-scaling of p_0, however, the minijet cutoff scale in AA collisions (p_0^{AA}) at LHC energies becomes significantly higher and thus σ_{jet} becomes much smaller, as shown in Fig. 3 by the dashed line that is much lower than the dotted line at LHC energies. This leads to a significant decrease of the charge particle yields at LHC energies, especially for central AA collisions where the binary scaling of minijet productions makes them more sensitive to the minijet cutoff p_0.

For peripheral AA collisions however, we expect no need for the A-scaling of p_0, because participant nucleons there are near the edge of the nucleus and should be almost free of saturation effects. Since we have not implemented this impact parameter-dependent nuclear scaling of p_0 and the current A-scaling of Eq. (10) is only valid for central AA collisions, we show in Fig. 11 the LHC Pb + Pb results without using the A-scaling of p_0 (dot-dashed lines and dashed lines), which are more suitable for peripheral collisions. Indeed, we see that the AMPT results without the A-scaling of p_0 give higher charged particle yields and are closer to the experimental data for peripheral collisions than the AMPT results with A-scaling of p_0. Also note that, since we have found that the Lund b value is much smaller in central AA collisions than in pp collisions, the Lund b value should depend on the system size or centrality, and increasing its value for peripheral AA collisions (similar to pp collisions) could further improve the description of charged particle yields there.

We have seen that the minijet cutoff scale p_0 becomes increasingly large with energy and can be more than 4 or even 6 GeV/c. However, it is questionable to treat transverse momentum exchanges below such a high value of p_0 as soft physics with the Lund string fragmentation, while the production of charm particles is usually viewed as a perturbative-QCD process where the FONLL approach has been very successful [52]. Therefore, the two-component model such as HIJING may be problematic for the initial condition at very high energies. For example, the need for us to introduce the nuclear scaling of p_0 for AA collisions at LHC energies and above may indicate the importance of saturation physics for large systems at very high energies. In addition, the current parton cascade in the AMPT model only includes elastic parton scatterings [14]. However, inelastic parton interactions [53] affect the parton abundance and momentum spectrum at high energies, and these effects are expected to be energy- and centrality-dependent. Therefore, including inelastic parton scatterings should improve the physics of a multiphase transport model [54].

The updated AMPT model has not shown obvious phenomenological improvements over the previous AMPT model when compared with the experimental data in this study, except that the updated model uses the same Lund a value for pp and AA collisions at all energies and thus removes the uncertainty of this parameter present in the previous AMPT model. However, the updated AMPT model should be more robust in its physics because of its inclusion of modern parton PDFs in the nuclei. Therefore, we expect it to provide a better foundation for future model developments and also show improvements in certain observables such as heavy flavor productions [55].

V. SUMMARY

A multiphase transport model has been using the old Duke-Owens parton distribution functions for the free proton and a schematic nuclear shadowing parametrization. This leads to significant uncertainties in its ability to address heavy flavor and/or high-p_T particles, because they are produced by perturbative-QCD processes and thus directly depend on the parton distribution functions of nuclei. In this study, we have incorporated a newer set of free proton parton distribution functions, the CTEQ6.1M set, and the impact parameter-dependent EPS09sNLO nuclear shadowing in an updated AMPT model. We first determine the energy dependence of two key parameter functions, $p_0(s)$ and $\sigma_{\mathrm{soft}}(s)$, in the HIJING two-component model by fitting the experimental data on total and inelastic cross sections of pp and $p\bar{p}$ collisions from $\sqrt{s} \sim 4$ GeV to 13 TeV. We then compare particle productions from the string melting version of the updated AMPT model with the experimental data in both pp and AA collisions at RHIC and LHC energies. We find that the $p_0(s)$ function and the constant values for the Lund string fragmentation parameters that can reasonably describe the particle yields and p_T spectra in pp collisions fail to describe central AA collisions at LHC energies. Therefore, we introduce a nuclear scaling of the minijet transverse momentum cutoff p_0 for central AA collisions at high energies that is motivated by the color glass condensate picture. Then the string melting AMPT

model can also reasonably describe the overall particle yields and p_T spectra of AA collisions at both RHIC and LHC energies. We expect the updated AMPT model to provide more reliable descriptions of heavy flavor and high-p_T observables in relativistic collisions of both small and large systems. It also serves as a good foundation for further improvements of the model.

ACKNOWLEDGMENTS

[1] I. Arsene *et al.* (BRAHMS Collaboration), Nucl. Phys. A **757**, 1 (2005); B. B. Back *et al.* (PHOBOS Collaboration), *ibid.* **757**, 28 (2005); J. Adams *et al.* (STAR Collaboration), *ibid.* **757**, 102 (2005); K. Adcox *et al.* (PHENIX Collaboration), *ibid.* **757**, 184 (2005).

[2] U. Heinz and R. Snellings, Annu. Rev. Nucl. Part. Sci. **63**, 123 (2013).

[3] W. Busza, K. Rajagopal, and W. van der Schee, Annu. Rev. Nucl. Part. Sci. **68**, 339 (2018).

[4] Z. W. Lin, C. M. Ko, B. A. Li, B. Zhang, and S. Pal, Phys. Rev. C **72**, 064901 (2005).

[5] Z. W. Lin and C. M. Ko, Phys. Rev. C **65**, 034904 (2002).

[6] G. L. Ma and Z. W. Lin, Phys. Rev. C **93**, 054911 (2016).

[7] Y. He and Z. W. Lin, Phys. Rev. C **96**, 014910 (2017).

[8] L. Y. Zhang, J. H. Chen, Z. W. Lin, Y. G. Ma, and S. Zhang, Phys. Rev. C **98**, 034912 (2018).

[9] AMPT source codes are available at http://myweb.ecu.edu/linz/ampt/.

[10] X. N. Wang and M. Gyulassy, Phys. Rev. D **44**, 3501 (1991).

[11] M. Gyulassy and X. N. Wang, Comput. Phys. Commun. **83**, 307 (1994).

[12] J. Pumplin, D. R. Stump, J. Huston, H. L. Lai, P. M. Nadolsky, and W. K. Tung, J. High Energy Phys. 07 (2002) 012.

[13] I. Helenius, K. J. Eskola, H. Honkanen, and C. A. Salgado, J. High Energy Phys. 07 (2012) 073.

[14] B. Zhang, Comput. Phys. Commun. **109**, 193 (1998).

[15] B. A. Li and C. M. Ko, Phys. Rev. C **52**, 2037 (1995).

[16] E. Eichten, I. Hinchliffe, K. D. Lane, and C. Quigg, Rev. Mod. Phys. **56**, 579 (1984); **58**, 1065 (1986).

[17] T. K. Gaisser and F. Halzen, Phys. Rev. Lett. **54**, 1754 (1985).

[18] G. Pancheri and Y. N. Srivastava, Phys. Lett. B **182**, 199 (1986).

[19] D. W. Duke and J. F. Owens, Phys. Rev. D **30**, 49 (1984).

[20] Z. W. Lin, Indian J. Phys. **85**, 837 (2011).

[21] M. Gluck, E. Reya, and A. Vogt, Z. Phys. C **67**, 433 (1995).

[22] W. T. Deng, X. N. Wang, and R. Xu, Phys. Rev. C **83**, 014915 (2011).

[23] A. Accardi, L. T. Brady, W. Melnitchouk, J. F. Owens and N. Sato, Phys. Rev. D **93**, 114017 (2016).

[24] K. J. Eskola, H. Paukkunen, and C. A. Salgado, J. High Energy Phys. 04 (2009) 065.

[25] K. J. Eskola, H. Paukkunen, and C. A. Salgado, J. High Energy Phys. 07 (2008) 102.

[26] D. Stump, J. Huston, J. Pumplin, W. K. Tung, H. L. Lai, S. Kuhlmann, and J. F. Owens, J. High Energy Phys. 10 (2003) 046.

[27] X. N. Wang, Phys. Rev. D **43**, 104 (1991).

[28] Z. W. Lin, Phys. Rev. C **90**, 014904 (2014).

[29] V. Khachatryan *et al.* (CMS Collaboration), Phys. Rev. Lett. **105**, 022002 (2010).

[30] G. J. Alner *et al.* (UA5 Collaboration), Z. Phys. C **33**, 1 (1986).

[31] F. Abe *et al.* (CDF Collaboration), Phys. Rev. D **41**, 2330 (1990).

[32] W. Thome *et al.* (Aachen-CERN-Heidelberg-Munich Collaboration), Nucl. Phys. B **129**, 365 (1977).

[33] V. Khachatryan *et al.* (CMS Collaboration), Phys. Lett. B **751**, 143 (2015).

[34] C. Albajar *et al.* (UA1 Collaboration), Nucl. Phys. B **335**, 261 (1990).

[35] F. Abe *et al.* (CDF Collaboration), Phys. Rev. Lett. **61**, 1819 (1988).

[36] B. B. Abelev *et al.* (ALICE Collaboration), Eur. Phys. J. C **73**, 2662 (2013).

[37] J. Adam *et al.* (ALICE Collaboration), Phys. Lett. B **753**, 319 (2016).

[38] A. Aduszkiewicz *et al.* (NA61/SHINE Collaboration), Eur. Phys. J. C **77**, 671 (2017).

[39] A. Adare *et al.* (PHENIX Collaboration), Phys. Rev. C **83**, 064903 (2011).

[40] J. Adams *et al.* (STAR Collaboration), Phys. Lett. B **616**, 8 (2005).

[41] K. Aamodt *et al.* (ALICE Collaboration), Eur. Phys. J. C **71**, 1655 (2011).

[42] J. Adam *et al.* (ALICE Collaboration), Eur. Phys. J. C **75**, 226 (2015).

[43] A. M. Sirunyan *et al.* (CMS Collaboration), Phys. Lett. B **779**, 358 (2018).

[44] S. S. Adler *et al.* (PHENIX Collaboration), Phys. Rev. C **69**, 034909 (2004).

[45] B. I. Abelev *et al.* (STAR Collaboration), Phys. Rev. C **79**, 034909 (2009).

[46] B. Abelev *et al.* (ALICE Collaboration), Phys. Rev. C **88**, 044910 (2013).

[47] L. D. McLerran and R. Venugopalan, Phys. Rev. D **49**, 2233 (1994).

[48] K. Adcox *et al.* (PHENIX Collaboration), Phys. Rev. Lett. **88**, 242301 (2002).

[49] A. Adare *et al.* (PHENIX Collaboration), Phys. Rev. C **93**, 024901 (2016).

[50] K. Aamodt *et al.* (ALICE Collaboration), Phys. Rev. Lett. **106**, 032301 (2011).

[51] J. Adam *et al.* (ALICE Collaboration), Phys. Lett. B **772**, 567 (2017).

[52] M. Cacciari, S. Frixione, N. Houdeau, M. L. Mangano, P. Nason, and G. Ridolfi, J. High Energy Phys. 10 (2012) 137.

[53] Z. Xu and C. Greiner, Phys. Rev. C **71**, 064901 (2005).

[54] Z. W. Lin, Acta Phys. Polon. Supp. **7**, 191 (2014).

[55] L. Zheng, C. Zhang, S. Shi, and Z. W. Lin (unpublished).